A Development Study of a New Bi-directional Solenoid Actuator for Active Locomotion Capsule Robots

Wu, Linlin; Lu, Kaiyuan

Published in:
Electronics (Switzerland)

DOI (link to publication from Publisher):
10.3390/electronics9050736

Publication date:
2020

Document Version
Publisher's PDF, also known as Version of record

electronics

MDPI

Article

A Development Study of a New Bi-directional Solenoid Actuator for Active Locomotion Capsule Robots

Linlin Wu and Kaiyuan Lu *

The Department of Energy Technology, Aalborg University, 9220 Aalborg East, Denmark; lwu@et.aau.dk
* Correspondence: klu@et.aau.dk; Tel.: +45-3062-2569

Received: 27 February 2020; Accepted: 25 April 2020; Published: 29 April 2020

Abstract: A new bi-directional, simple-structured solenoid actuator for active locomotion capsule robots (CRs) is investigated in this paper. This active actuator consists of two permanent magnets (PMs) attached to the two ends of the capsule body and a vibration inner mass formed by a solenoidal coil with an iron core. The proposed CR, designed as a sealed structure without external legs, wheels, or caterpillars, can achieve both forward and backward motions driven by the internal collision force. This new design concept has been successfully confirmed on a capsule prototype. The measured displacements show that its movement can be easily controlled by changing the supplied current amplitude and frequency of the solenoid actuator. To validate the new bi-directional CR prototype, various experimental as well as finite element analysis results are presented in this paper.

Keywords: robotic endoscopy; endoscopic capsule robots; bi-directional active locomotion; solenoid actuator

1. Introduction

In recent years, several technologies [1–6] have been studied for promoting the development of capsule endoscopes, since its first generation was proposed by Given Imaging Ltd. in 2000 for inspecting small intestinal diseases [1]. The endoscopic capsule, as a revolutionary medical device, was proposed to achieve advanced diagnostic and treatment functionalities for the small bowel tract, where conventional tethered flexible endoscopes are only partially able to access. Although some commercial capsule products have already been applied in clinical practice, e.g., PillCam®by Medtronic Inc. (Minneapolis, MN, USA), EndoCapsule by Olympus Corp. (Tokyo, Japan), and MiroCam®by IntroMedic Co., Ltd. (Seoul, Korea), they are propelled through the gastrointestinal (GI) tract in a passive manner, purely depending on peristalsis contractions of the digestive lumen. Due to the lack of an active and controllable locomotion mechanism in the conventional capsule endoscope to steer the scope in desired areas of the GI tract for accurate and double inspections, false negative results may occur, reducing the effectiveness and reliability in clinical practice [7].

In order to meet the demands of accurate positioning and controllable locomotion, an active actuator system is needed to be embedded in the robotic capsule endoscope. This enables the doctors to operate the capsule at any desired locations and, if necessary, to invert the direction for double inspections. Active capsule robots (CRs), as a promising technology, have become a common pursuit of endoscopists and biorobotic engineers [8]. Furthermore, active CRs can also perform some additional desired functions, such as screening, biopsy, and drug delivery in the future [9,10].

For actuator-driven surgical/capsule robots, with respect to their different design concepts, control methodology and modelling, some review papers on fluidic actuator-, magnetic actuator-, smart material actuator-, and cable-driven mechanism-based CRs have been reported over the past two

decades [11–16]. In brief, the reported flexible fluidic actuator needs to be operated with a high pressure [11,14]. The smart material actuators, i.e., shape memory alloys (SMAs) and piezoelectric actuators, normally work at high temperature or high voltage [13,16], and they have relative complex structures as well as material fatigue and high-cost problems [11]. External magnetic fields may be used to interact with the capsule side magnet to achieve locomotion. The advantage is that there is no power consumption on the CR side for locomotion. The disadvantage of this method is that the magnetic force exerted on the CR drops dramatically, when the distance between the external magnet and the CR side magnet increases. Additionally, due to the strong attractive force between the magnets, the CR side magnet always tends to travel towards the external magnet, resulting in a strong force applied on the body tissue, increasing the friction as well [5,16]. Such a method may be more suitable to trigger an action, such as opening the inflation valve [17,18] or controlling the needle for biopsy [19], than active locomotion.

For controllable locomotion, CRs are often designed with the aid of motors integrated in different mechanisms, such as elastic-legged, paddle-type, tank-like type, spiral, and vibration-type CRs. The legged-locomotion CR shown in [20,21] achieves a bi-directional movement by driving its super-elastic legs using two internal DC brushless motors. However, these two internal motors for driving external legs occupy a large space inside the capsule and cause a significant power consumption, resulting in a capsule with dimensions that are not compatible for ingestion. In [22], a paddle-based CR is studied, but it can move in a single direction only. The propulsion of the multi-paddle comes from the interaction force between a linear actuator and two mobile cylinders. In [23–25], a tank-like CR is proposed, equipped with micropatterned treads driven by a DC motor that may help reduce the damage to human tissue compared to other devices having external protruding structures. However, this tank-like CR is specifically designed for the colon, which has a larger dimension than that of the intestine; moreover, the on-board power unit is still a challenge to power the internal six motors simultaneously. In [26], a CR fabricated with a rotary spiral-shaped body is excited by a brushless DC motor. A vibration-based CR actuated by centripetal force, which is generated by a vibratory motor, is also mentioned. However, both the spiral and the vibratory locomotion CRs may lead to possible drawbacks, such as structure complication and integration complexity, due to the use of a separate motor as the main driving unit.

Furthermore, an inchworm-inspired CR is presented in [27–31]. A worm-like robot driven by a geared DC motor is described in [27,28]. A mesh worm-like, multi-segment CR mentioned in [29] is driven by shortening or extending the tendons as the motors rotate. An inchworm-like CR achieves forward or backward motions by its front and rear clampers, which are driven by DC motors [30]. However, some drawbacks, such as low travelling speed compared with CRs having external legs or paddles and large volume due to the equipped motors, limit the applications of this type of CR.

In this paper, a new actuator applied to a bi-directional locomotion-based linear active CR is presented. The propulsion of the CR is produced by the collision action between the internal moving mass and the permanent magnets (PMs) located on the end plates. The vibration of the inner mass is excited by an alternating current supplied to the small coil. This current is formed in such a way that a half-cycle positive rectangular current is combined with a half-cycle negative sinusoidal current. The net displacement of the CR in one cycle is the difference between its forward and backward displacements experienced in one current period. To overcome natural peristalsis, when fixed at the desired position, an external large PM may be employed to anchor the CR to perform accurate inspection or other treatments. Compared with the existing actuator designs, this new actuation method, adopting an internal collision force as the driving source, has a simple structure (no DC motors) to achieve bi-directional movements, while offering flexibilities in speed/displacement control by varying the current amplitude and frequency.

In Section 2 of this paper, the new CR is proposed and described, detailing its mechanical structure (Section 2.1) and working principle (Section 2.2). The finite element analysis and simulated results

are presented in Section 3, whereas in Section 4, various experimental results are provided. Finally, Section 5 concludes this paper with future perspectives of this work.

2. New Bi-directional Locomotion CR

2.1. Mechanical Structure and Components

The new active actuation mechanism proposed in this paper consists of two cylindrical PMs attached to the two ends of the CR, and one inner mass moving between the two inserted PMs, as shown in Figure 1. The detailed components of the inner mass can be seen on the right side of Figure 1, including a small solenoid coil with an inserted iron core and two gaskets. For the two PMs, namely PM1 and PM2, they face each other with the same polarity (south pole). This actuator is excited by the wired current, but it will be further miniaturized to be a wireless actuator in the future. Compared with the existing actuators, this CR can move with a controllable speed and displacement by simply adjusting the frequency and/or the amplitude of the supplied current. In additional, the advantage of having a simple structure for this active actuator makes it possible for a compact and embeddable design of the CR.

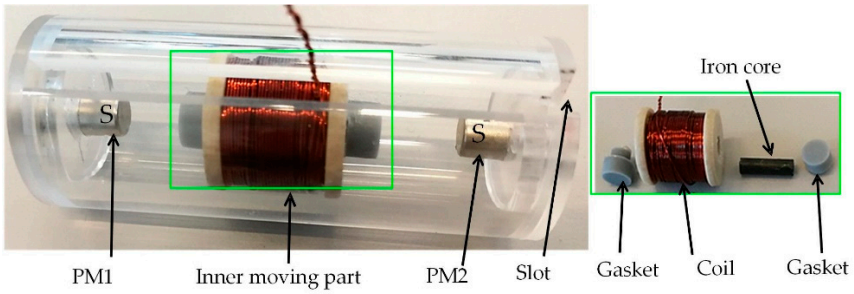

Figure 1. Structure and components of the new bi-directional active locomotion actuator.

2.2. Active Actuation Principle

The schematic diagram showing the working principle of the new actuator, as well as the CR locomotion steps for a single cycle, are shown in Figure 2. The propulsion of the CR is produced by the collision action between the internal moving mass and the end PM, occurring when the small coil, supplied with alternating currents, moves between the two PMs. This current has a special waveform, i.e., the half-period has a positive rectangular current waveform, while the other half has a negative sinusoidal current waveform. Once this kind of current is supplied to the small coil, an unbalanced electromagnetic force appears, resulting from the interaction between the magnetic field produced by the small coil current and the two PMs. This force acts on the entire inner mass and drives the small coil to move towards one of the PMs. While moving towards the PM, the small coil is kept accelerated until it collides with the PM. In a complete period, the small coil collides twice with the end-plate PMs. The collision force acting on the CR is able to drive the whole CR to move forward or backward. The net displacement of the CR in one cycle is determined by the difference between its forward and backward displacements. The different steps of the CR active locomotion mechanism are illustrated in Figure 2 and described below.

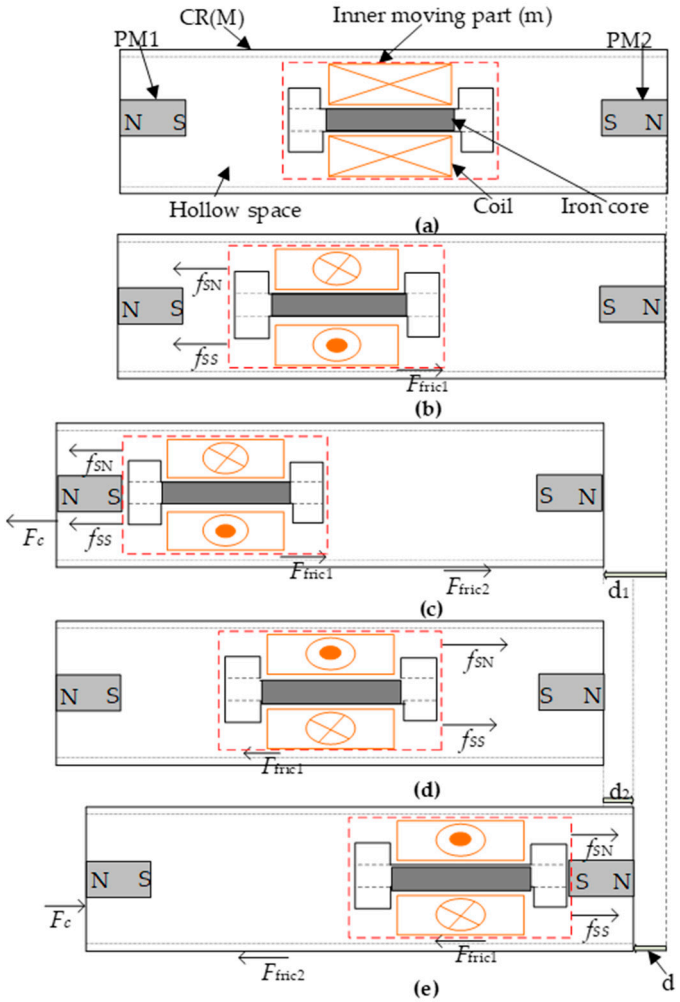

Figure 2. Representation of different steps of the capsule robot (CR) locomotion mechanism: (**a**) original position, (**b**) coil begins to move towards PM1, (**c**) coil collides to PM1 and drives the capsule to move forward, (**d**) coil moves back to PM2, (**e**) coil collides to PM2 and drives the capsule to move backward.

- Step 1. The coil is originally located at the center of the CR (Figure 2a), and meanwhile the supplied current to the coil is zero. Since a balanced force is acting on the coil by the two PMs, the coil as well as the CR body remain still.
- Step 2. When a positive rectangular shape current is supplied to the small coil, both the attractive force f_{SN} between PM1 and the energized coil and the repelling force f_{SS} between PM2 and the coil are in the same direction. The total force overcomes the frictional force F_{fric1} and drives the small coil to move towards PM1 (Figure 2b). During this process, the reaction force acting on the CR body is insufficient to overcome the external frictional force between the CR body and its contact surface, and therefore the CR remains still as shown in Figure 2b.
- Step 3. Since the small coil is kept accelerated when moving towards PM1, it slams into PM1 with a large velocity. As a consequence, the instantaneous collision force *Fc*, which is generated by the collision action, acts on the CR body and drives the CR to move forward, overcoming the external frictional force F_{fric2} (Figure 2c). Finally, the CR as well as the inner mass stop at a new position and thus the forward displacement d_1 of the CR is achieved (Figure 2c).
- Step 4. Upon reversing the current direction, and comparison with the forces described in Figure 2b, the directions of the interaction forces between the small coil and the two inserted PMs as well as the friction force F_{fric1} are reversed, as illustrated in Figure 2d. Consequently, the locomotion direction of the small coil is also reversed.

- Step 5. Similar to the descripted procedure in step 3, the opposite collision force then drives the CR to move backward and stop at another new position. The backward displacement of the CR in this process is denoted as d_2 (Figure 2e), which is smaller than d_1 since the negative current waveform is chosen to be sinusoidal instead of rectangular. Therefore, the net CR displacement in one cycle can be depicted as the displacement difference between its forward and backward displacements, namely:

$$d = d_1 - d_2, \tag{1}$$

Since periodic asymmetrical AC current is supplied to the coil, the coil thus performs the reciprocating oscillation inside the CR. As can be observed in Figure 2, the net displacement of the CR in one cycle is calculated by the displacement difference between the forward and backward displacements, which can be controlled by the amplitude of the supplied current. The frequency of the supplied current determines how often this net displacement may repeat itself, determining the moving speed of the CR.

3. Finite Element Modelling and Analysis

A finite element model (FEM) adopted to simulate the CR prototype was performed with COMSOL Multiphysics software (Stockholm, Sweden), and the model parameters are given in Table 1. A 3D model with a DC current in the small coil was studied, and the corresponding magnetic flux density when the small coil parked at a position of Z = 21 mm is shown in Figure 3 as an example.

Table 1. Parameters of the finite element model (FEM) analysis according to the capsule prototype.

Parameter	Value	Unit
coil inner radius	2	mm
coil thickness	3.5	mm
coil length	12	mm
magnet radius	2.5	mm
magnet length	10	mm
magnet remanence	1.074	T
iron mass	0.362	g
iron diameter	3	mm
iron height	12	mm
inner mass (m)	9.36	g
total capsule mass (M)	27.15	g
capsule length	60	mm
capsule inner diameter	12	mm
capsule outer diameter	14	mm

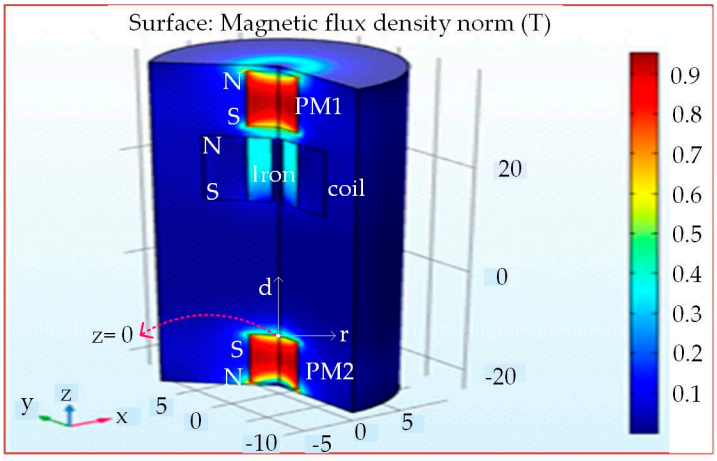

Figure 3. 3D Finite Element Model (FEM) of the CR.

The driving force acting on the coil, including the attractive/repelling force between the coil with an iron core and the two end PMs, can be calculated using the FEM analysis. Different driving force profiles, as shown in Figure 4, are obtained when the coil, supplied with different constant currents, moves between the two end PMs. These force profiles can be used to calculate the real-time force acting on the small coil as the supplied current and position of the small coil vary in the required forms.

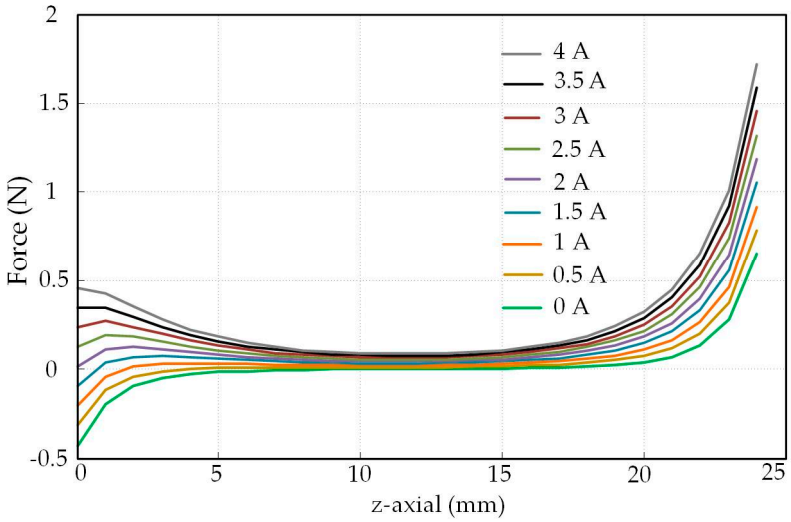

Figure 4. The resultant force acting on the coil under different currents.

As can be observed in Figure 4, the driving force, acting on the small coil at a certain position, increases when the supplied current is increased. For a constant current, when the coil moves from PM2 to PM1 ($Z = 0$ to $Z = 24$ mm), the force is significantly increased when approaching PM1 for a positive current. This is because of the forces generated by the interaction between the coil magnetic field produced by a positive current and the two magnets are always along the positive z-axis towards PM1. The attracting force between PM2 and the coil iron core is along the negative z-axis, whereas the attracting force between PM1 and the iron core is along the positive z-axis (e.g., this can be observed in Figure 4 from the curve with 0 A current). Therefore, the total force shows such a profile, as illustrated in Figure 4.

Based on the force profiles shown in Figure 4 for different DC current values, the actual force acting on the coil in one cycle could then be obtained by using the real current waveform to search for the corresponding force waveform, which is shown in Figure 5a. The position change of the coil with respect to the $Z = 0$ point, as indicated in Figure 3, is given in Figure 5b. The supplied current is a combination of a positive half-cycle rectangular shape waveform followed by a negative half-cycle sinusoidal waveform. It can be observed that a large acceleration force can be quickly established to accelerate the small coil. At about 0.13 s, the displacement Z has reached 24 mm, meaning the coil is now touching PM1.

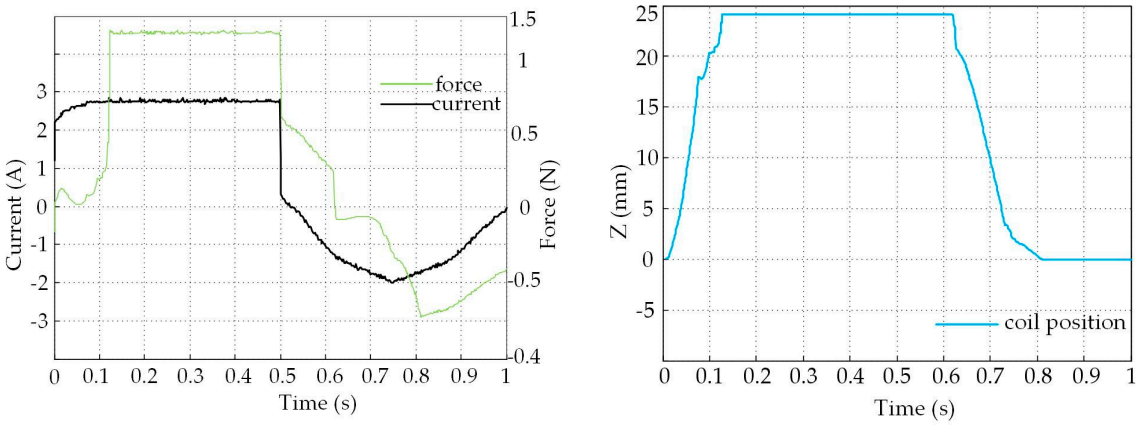

(**a**) (**b**)

Figure 5. The force acting on the coil corresponding to the excited pulsed current in one period, (**a**) the force and current profiles; (**b**) the coil displacement.

The force is kept constant until the coil performs the reversed motion. For the negative half-cycle sinusoidal current in the remaining period, the reversed force actuates the coil to move from PM1 to PM2. It can be observed that it takes much longer to return the coil to its original position, meaning that the acceleration achieved by the coil during this reversed moving period is smaller than that achieved during the forward acceleration period. Unbalanced acceleration results in unbalanced forward and backward movements, producing a useful net displacement.

Magnetic permeability of the core inserted in the coil affects the force used to drive the coil to move forward. As can be observed in Figure 6, a quite different flux pattern can be seen when changing the iron core (with a relative permeability of 4000) to air (with a relative permeability of 1). The finite element simulation results indicate that reducing the core permeability reduces the interaction force between the coil and PM2, from 0.875 N (iron core) to 0.122 N (air core), for example. It is preferable to use high permeability material like iron.

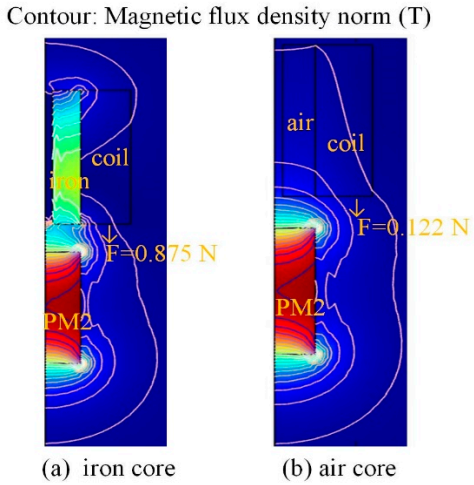

Figure 6. Magnetic flux contour under different magnetic permeabilities of the inserted core: (**a**) iron core; (**b**) air core.

4. Experimental Setup and Results

4.1. Experimental Setup

To measure the proposed CR displacements under various supplied currents, an experimental platform was set up, as shown in Figure 7. This platform consisted of the CR prototype and an optoNCDT 1420 Laser Sensor (MICRO-EPSILON MESSTECHNIK GmbH & Co. KG, Königbacher Straße 15, Ortenburg, Germany). In addition, the experimental platform also enabled the authors of this paper to measure the displacement of the small coil in one cycle. Comparing the CR displacement with the small coil displacement in the same coordinate system, it helps to clarify the driving concept of the proposed CR.

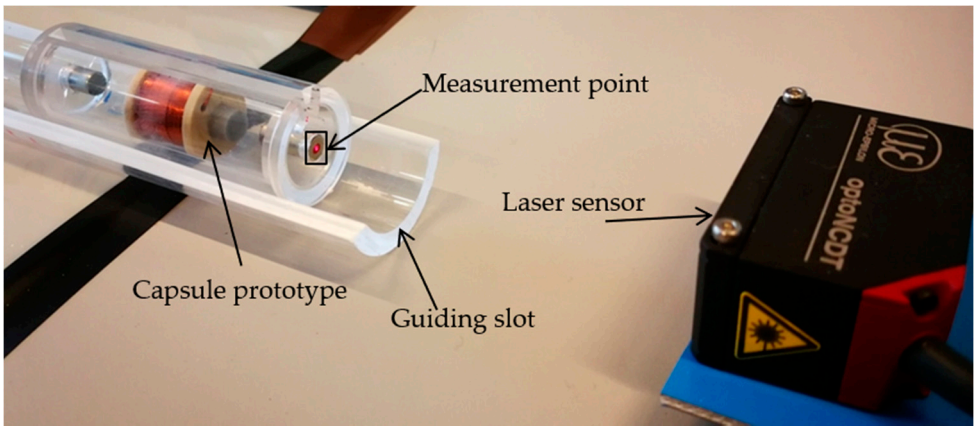

Figure 7. Experimental setup.

4.2. Experimental Results and Analysis

The progress of the capsule motion is illustrated in Figure 8. Figure 8a is the original parking position, as in Figure 2a. The two end places are marked as P1 and P2, respectively. Next, the coil is energized and is moved to the left magnet (as in Figure 2b,c). As the coil punches the magnet, a large collision force is generated and the capsule is pushed to position P2′ (Figure 8b). Then, the current direction is reversed, the coil leaves the left magnet, and, during this coil movement, the capsule remains still (Figure 8c, as in Figure 2d). Once the coil hits the right-side magnet, the collision force drives the capsule to move to the right position P1′ (Figure 8d), and a smaller displacement in this process is achieved (as Figure 2e), due to different current profiles as discussed previously. Finally, the net displacement of the capsule in one cycle is thus achieved and marked as X in Figure 8d.

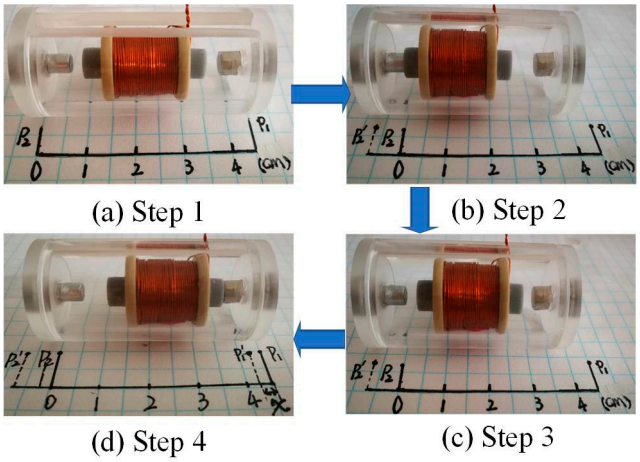

Figure 8. The locomotion progress pictures of the proposed CR prototype in one cycle.

The displacements of the CR under various current profiles are measured by the laser sensor. According to the locomotion principle of the CR, the bi-directional displacements of the CR and the coil in five cycles were measured, and are shown in Figures 9 and 10, respectively. It can be clearly observed from the graphs shown in Figure 9 that the CR achieved a net forward displacement in each cycle driven by the oscillating coil. The coil first moves forward, driven by the supplied rectangular shape current. Then, the coil collides with the CR and drives the CR to move forward. The measured CR as well as the coil displacements in this half-cycle are shown as positive displacements in Figure 9. Similar to the locomotion mechanism described in the first half-cycle, if the current supplied to the coil is reversed in the remaining half-cycle, the displacements of the CR and the coil move in the opposite direction, as indicated in Figure 9. Thus, the net forward displacement of the CR is the displacement difference between its bi-directional movements in one cycle. Similar to the forward locomotion profile analyzed above, the backward locomotion of the CR is experimentally demonstrated by changing the supplied current direction, as shown in Figure 10.

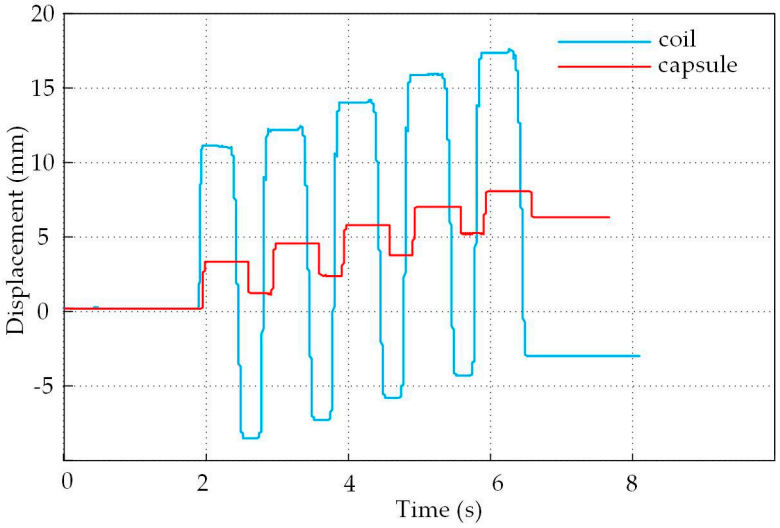

Figure 9. The forward displacements of the CR and the small coil.

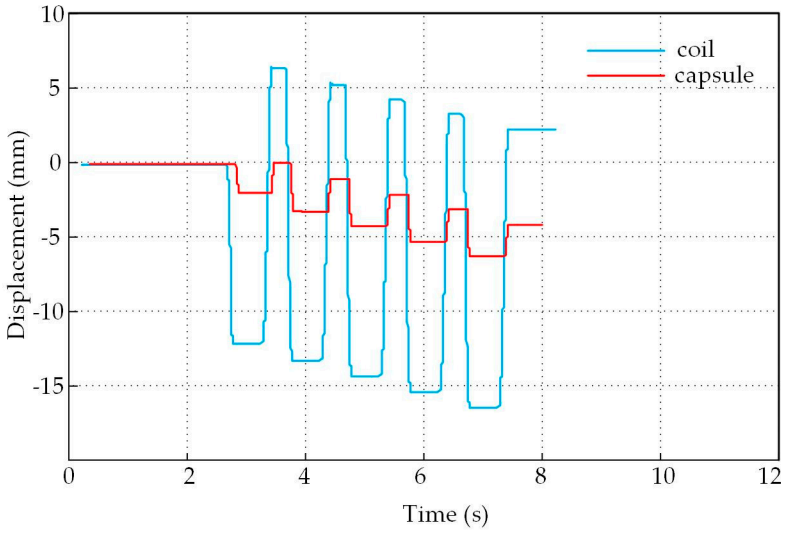

Figure 10. The backward displacements of the CR and the internal coil.

To study the locomotion principles of both the CR and the coil in detail, the displacement profiles of the coil and the CR in one cycle were recorded, together with the supplied AC current profile and the corresponding force acting on the coil. These profiles are shown in Figure 11. The displacements

are shown in the local coordinate system relative to one end of the capsule. The blue curve in Figure 11 represents the coil displacement in one cycle, the red one is the CR displacement, the dark blue line recorded by an oscilloscope is the supplied current, and the green line is the corresponding force profile obtained from the FEM.

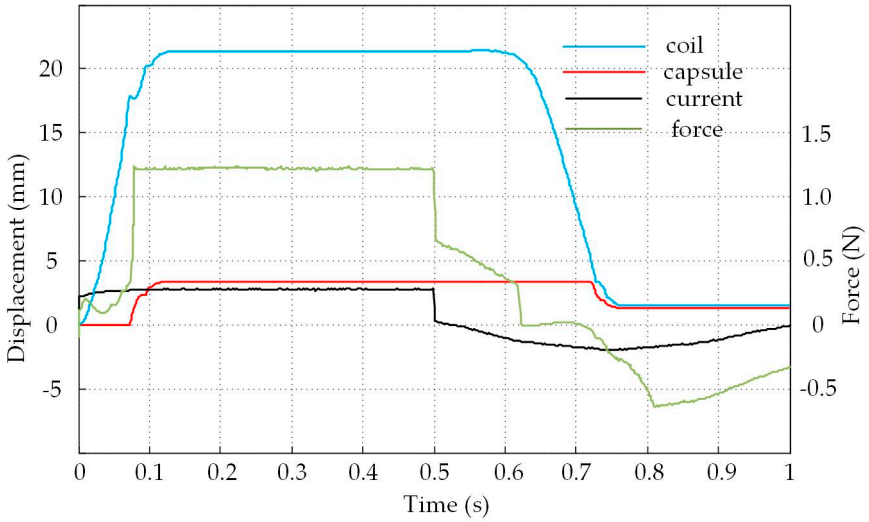

Figure 11. Measured current profile, coil, and capsule displacement waveforms in one period.

In the beginning, as the current is quickly established to a DC value, the coil starts to move away from its parked position at $Z = 0$ mm. The coil in this process is kept accelerated so that the small coil can collide with the PM1 at a high speed, and the coil and capsule move forward together (Figure 11). The acceleration process of the coil obeys Newton's second law of motion. Collision of the coil, traveling at a high speed with the stationary PM1, obeys the law of momentum conservation, i.e., the coil mass times its velocity is equal to the total mass of the CR times the capsule velocity. The kinetic energy gained in the coil during the acceleration process is suddenly released upon collision. The large force, which enables the capsule to be driven forward, is then generated after the collision action. During the progress of forward movement of the capsule, the external frictional force decelerates the capsule and stops it at a distance of d_1 (Figure 2c) with the small coil attached to PM1. At the end of the first half-cycle, the current in the coil begins to change to a negative sinusoidal current. The displacement curve of the coil (blue line) indicates that the coil does not immediately perform the reversed movement when it is supplied with the reversed current, since the current is slowly built up and the generated force in the beginning is not enough to overcome the attractive force between the coil iron core and PM1. The negative sinusoidal current gradually increases, resulting in a slow increase in the reversed driving force. When the current is high enough and the small coil starts the reversed motion, similar to the process described in the first half-cycle, the small coil performs a reversed acceleration towards PM2 and until the collision with PM2 happens. Therefore, the CR is driven to move backward and finally stops at the reversed displacement of d_2 (Figure 2d).

4.3. Analysis of The Displacement and Speed Control Abilities

As mentioned above, the CR displacement is affected by the supplied current in the small coil. In general, this kind of AC current has three key design parameters, i.e., current frequency as well as positive and negative current amplitudes. To further study the influences of these three parameters on the capsule displacement performance, the CR displacements were measured under different current frequencies and amplitudes, as shown in Figures 12–14. In addition, the frictional force of the contact surface, which also affects the CR displacement, is changed by using different surface materials, and the corresponding measured average net displacements are given in Table 2.

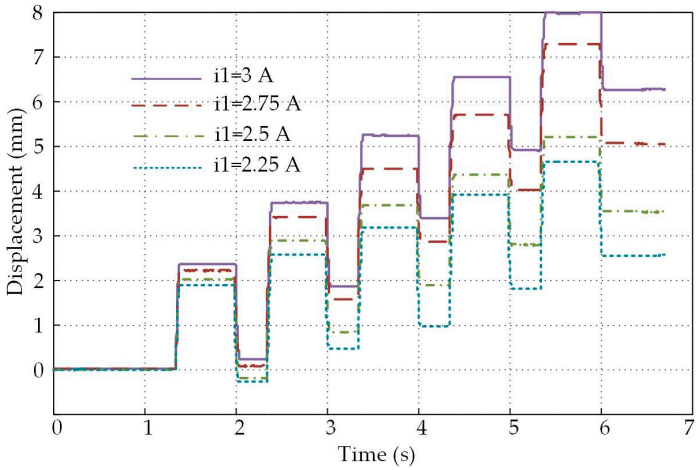

Figure 12. CR displacement vs. positive current amplitude.

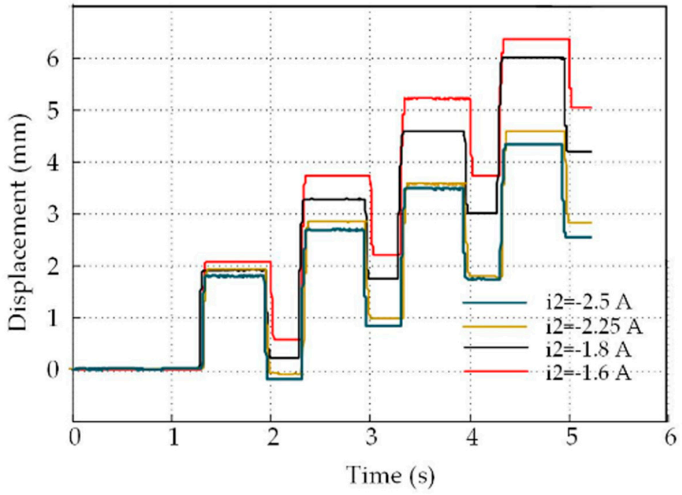

Figure 13. CR displacement vs. negative current amplitude.

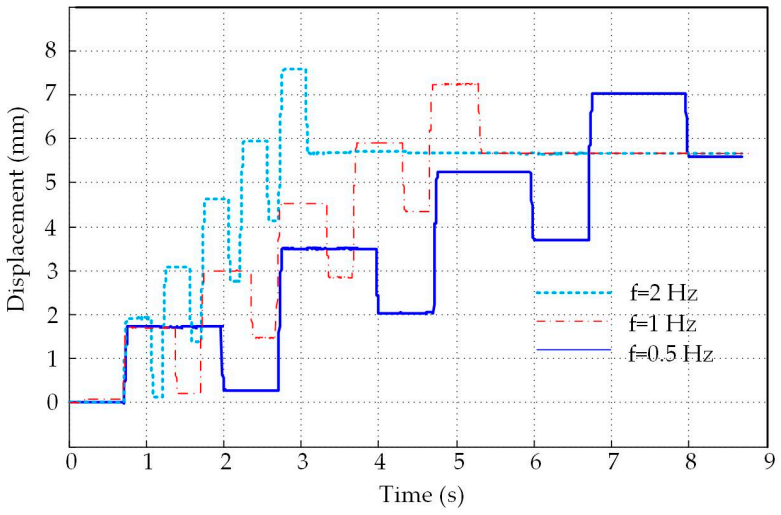

Figure 14. CR displacement vs. current frequency.

Table 2. CR displacements measured under different contact surfaces.

Contact Material	Acrylic	Paper	Sandpaper
Net displacement (mm)	0.58	0.49	0.4

Figure 12 shows the CR displacements in five cycles measured under different positive current amplitudes ranging from 2.25 A to 3 A. A constant negative current amplitude of 2 A and a constant current frequency of 1 Hz were used. As can be observed in Figure 10, although the positive rectangular current and the negative sinusoidal current have the same half-period duration, the step forward movement of the capsule has a larger duty ratio than that in the backward movement. This occurs because, for the negative sinusoidal current, the current increases slowly and the duration for the current range that is high enough to drive the capsule backward is shortened. In the positive rectangular current period, the current is established to its desired DC value quickly, and the capsule starts to move almost immediately after the rectangular current is supplied. In addition, this figure also illustrates that the CR displacement shows a clear increase when the current amplitude is increased. On average, when the current amplitude is increased by 0.25 A, the displacement is increased by 1.25 mm after 5 cycles.

Similarly, the same AC current waveform was supplied to the small coil, while its negative current amplitude was varied. The CR displacements were measured under various negative current amplitudes, and the results are given in Figure 13. This figure indicates that the displacement of the CR decreases as the amplitude of the negative current increases, while its positive current amplitude is kept at 2.75 A. Therefore, the net CR displacement decreases when the negative amplitude increases. However, a minimum value of the amplitude of the negative current exists, below which the generated force by the coil current is not large enough to overcome the attractive force between PM1 and the coil iron to start the reversed acceleration.

In Figure 14, the CR displacements are measured under various current frequencies while keeping the positive and negative current amplitudes constant (i.e., 2.75 A and −2 A, respectively). The light blue dashed line represents the CR displacement measured under the frequency of 2 Hz, whereas the red dashed line is the measured displacement under 1 Hz and the blue line displacement is achieved under 0.5 Hz. Figure 14 indicates that the current frequency directly affects the travelling speed of the capsule. The larger the current frequency, the shorter the time needed for the CR to reach the same displacement. By varying the frequency of the current, the travelling speed of the CR can be easily controlled.

The above experiments validated the feasibility of the proposed new structure and locomotion mechanism, demonstrating its bi-directional moving ability and changeable net displacement as well as moving speed, obtained by varying the current amplitude and frequency. However, the lab test environment is rather ideal with the external frictional property being uniform. The situation inside the human body is more complex. The variation of the friction affects the displacement of the capsule. For a quick demonstration of this point, materials with different frictional properties (acrylic tube, paper, sandpaper) were used as the external contact surface. The measured average displacements are given in Table 2. It was reported in [32] that the average frictional resistance between the capsule and small intestine wall is 20–50 mN. The sliding frictional force provided by the normal paper and the acrylic surface is around 70 mN and 50 mN, respectively. The sliding frictional force provided by the sandpaper is the highest. It can be observed from Table 2 that the average measured net displacement of the CR decreases when the friction increases, which is as expected. As mentioned previously, the driving force is provided by the collision of the coil traveling at a high speed with the stationary capsule. The displacement of the capsule after collision obeys Newton's second law of motion. This implies that the generated driving force at the collision moment is much larger than the external frictional force against capsule displacement, so the increased frictional force does not significantly reduce the net displacement.

5. Discussion and Conclusions

This paper presents a new active actuator mechanism for bi-directional capsule robot applications. The new CR structure and driving concept were validated experimentally on a prototype. The driving principle of the CR was to utilize the internal collision force between the inner moving mass and the CR body. In comparison with existing driving mechanisms, this new mechanism has a simple structure and its net displacement and travelling speed can be controlled by simply varying the current amplitude and frequency.

The supplied current has a special waveform, combining a half-period positive rectangular current waveform with a half-period negative sinusoidal current waveform. This makes it possible to accelerate the small coil differently before it collides with the two end PMs, achieving a bi-directional movement ability. The experimental results also demonstrated that this prototype can be easily controlled to achieve different forward/backward displacements and traveling speeds.

Although the proposed new actuation principle was experimentally validated with demonstrations of variable displacement and moving speeds, it should be tested in a more complex environment that can mimic the conditions inside the human body. This is considered as important future work for the next step of the research.

Author Contributions: Conceptualization, L.W. and K.L.; Methodology, L.W. and K.L.; Validation, L.W.; Writing—original draft preparation, L.W.; writing—review and editing, K.L. and L.W. All authors have read and agreed to the published version of the manuscript.

Funding: This research received no external funding.

Conflicts of Interest: The authors declare no conflict of interest.

References

1. Iddan, G.; Meron, G.; Glukhovsky, A.; Swain, P. Wireless capsule endoscopy. *Nature* **2000**, *405*, 417. [CrossRef] [PubMed]
2. Basar, R.; Ahmad, Y.; Cho, J.; Ibrahim, F. An Improved Wearable Resonant Wireless Power Transfer System for Biomedical Capsule Endoscope. *IEEE Trans. Ind. Electron.* **2018**, *65*, 7772–7781. [CrossRef]
3. Ciuti, G.; Menciassi, A.; Dario, P. Capsule endoscopy: From current achievements to open challenges. *IEEE Rev. Biomed. Eng.* **2011**, *4*, 59–72. [CrossRef] [PubMed]
4. Gao, M.; Hu, C.; Chen, Z.; Zhang, H.; Liu, S. Design and fabrication of a magnetic propulsion system for self-propelled capsule endoscope. *IEEE Trans. Biomed. Eng.* **2010**, *57*, 2891–2902. [PubMed]
5. Liu, L.; Towfighian, S.; Hila, A. A review of locomotion systems for capsule endoscopy. *IEEE Rev. Biomed. Eng.* **2015**, *8*, 138–151. [CrossRef]
6. Kim, B.; Park, S.; Park, J. Microrobots for a capsule endoscope. In Proceedings of the IEEE/ASME 2009 International Conference on Advanced Intelligent Mechatronics, Singapore, 14–17 July 2009; pp. 729–734.
7. Rondonotti, E.; Herrerias, J.M.; Pennazio, M.; Caunedo, A.; Mascarenhas-Saraiva, M.; de Franchis, R. Complications, limitations, and failures of capsule endoscopy: A review of 733 cases. *Gastrointest. Endosc.* **2005**, *62*, 712–716. [CrossRef]
8. Meng Max, Q.H.; Mei, T.; Pu, J.; Hu, C.; Wang, X.; Chan, Y. Wireless robotic capsule endoscopy: State-of-the-art and challenges. In Proceedings of the Fifth World Congress on Intelligent Control and Automation, Hangzhou, China, 5–19 June 2004; pp. 5561–5565.
9. Sliker, L.J.; Ciuti, G. Flexible and capsule endoscopy for screening, diagnosis and treatment. *Expert Rev. Med. Devices* **2014**, *11*, 649–666. [CrossRef]
10. Lee, H.J.; Choi, N.; Yoon, E.S.; Cho, I.J. MEMS devices for drug delivery. *Adv. Drug Deliv. Rev.* **2018**, *128*, 132–147. [CrossRef]
11. Le, H.; Do, T.; Phee, S. A survey on actuators-driven surgical robots. *Sens. Actuators A Phys.* **2016**, *247*, 323–354. [CrossRef]
12. Catherine, J.; Rotinat-Libersa, C.; Micaelli, A. Comparative review of endoscopic devices articulations technologies developed for minimally invasive medical procedures. *Appl. Bionics Biomech.* **2011**, *8*, 151–171. [CrossRef]

13. Cisse, C.; Zaki, W.; Ben Zineb, T. A review of constitutive models and modelling techniques for shape memory alloys. *Int. J. Plast.* **2016**, *76*, 244–284. [CrossRef]
14. De Greef, A.; Lambert, P.; Delchambre, A. Towards flexible medical instruments: Review of flexible fluidic actuators. *Precis. Eng.* **2009**, *33*, 311–321. [CrossRef]
15. Sliker, L.; Ciuti, G.; Rentschler, M.; Menciassi, A. Magnetically driven medical devices: A review. *Expert Rev. Med. Devices* **2015**, *12*, 737–752. [CrossRef] [PubMed]
16. Zhao, D.; Guo, Y.; Peng, C. Review of the active locomotion system for capsule endoscope. *J. Biomed. Eng.* **2010**, *27*, 215–218.
17. Do, T.; Seah, T.; Yu, H.; Phee, S. Development and Testing of a Magnetically Actuated Capsule Endoscopy for Obesity Treatment. *PLoS ONE* **2016**, *11*, e0151711.
18. Do, T.; Ho, K.; Phee, S. A Magnetic Soft Endoscopic Capsule-Inflated Intragastric Balloon for Weight Management. *Sci. Rep.* **2016**, *6*, 39486. [CrossRef]
19. Son, D.; Dogan, M.; Sitti, M. Magnetically actuated soft capsule endoscope for fine-needle aspiration biopsy. In Proceedings of the 2017 IEEE International Conference on Robotics and Automation (ICRA), Singapore, 29 May–3 June 2017; pp. 1132–1139.
20. Valdastri, P.; Webster, R.; Quaglia, C.; Quirini, M.; Menciassi, A.; Dario, P. A New Mechanism for Mesoscale Legged Locomotion in Compliant Tubular Environments. *IEEE Trans. Robot.* **2009**, *25*, 1047–1057. [CrossRef]
21. Quirini, M.; Menciassi, A.; Scapellato, S.; Dario, P.; Rieber, F.; Ho, C.-N.; Schostek, S.; Schurr, M. Feasibility proof of a legged locomotion capsule for the GI tract. *Gastrointest. Endos.* **2008**, *67*, 1153–1158. [CrossRef]
22. Carta, R.; Sfakiotakis, M.; Pateromichelakis, N.; Thone, J.; Tsakiris, D.P.; Puers, R. A multi-coil inductive powering system for an endoscopic capsule with vibratory actuation. *Sens. Actuators A Phys.* **2011**, *172*, 253–258. [CrossRef]
23. Sliker, L.J.; Kern, M.D.; Rentschler, M.E. An automated traction measurement platform and empirical model for evaluation of rolling micropatterned wheels. *IEEE/ASME Trans. Mechatron.* **2015**, *20*, 1854–1862. [CrossRef]
24. Sliker, L.; Kern, M.; Schoen, J.A.; Rentschler, M.E. Surgical evaluation of a novel tethered robotic capsule endoscope using micro-patterned treads. *Surg. Endosc.* **2012**, *26*, 2862–2869. [CrossRef] [PubMed]
25. Kim, D.; Lee, D.; Kim, B.; Lee, B.-I. A self-propelled robotic colonoscope using elastic caterpillars. In Proceedings of the 44th International Symposium on Robotics (ISR), Seoul, Korea, 24–26 October 2013; pp. 1–4.
26. Kim, Y.T.; Kim, D.E. Novel propelling mechanisms based on frictional interaction for endoscope robot. *Adv. Tribol.* **2010**, *53*, 203–211. [CrossRef]
27. Lin, W.; Shi, Y.; Jia, Z.; Yan, G. Design of a wireless anchoring and extending micro robot system for gastrointestinal tract. *Int. J. Med. Robot. Comput. Assisted Surg. MRCAS* **2013**, *9*, 167–179. [CrossRef] [PubMed]
28. Wang, K.; Yan, G.; Jiang, P.; Ye, D. A wireless robotic endoscope for gastrointestine. *IEEE Trans. Robot.* **2008**, *24*, 206–210. [CrossRef]
29. Bernth, J.E.; Arezzo, A.; Liu, H. A novel robotic mesh-worm with segment-bending anchoring for colonoscopy. *IEEE Robot. Autom. Lett.* **2017**, *2*, 1718–1724. [CrossRef]
30. Gao, J.; Yan, G. Locomotion analysis of an inchworm-like capsule robot in the intestinal tract. *IEEE Trans. Biomed. Eng.* **2016**, *63*, 300–310. [CrossRef]
31. Zarrouk, D.; Sharf, I.; Shoham, M. Conditions for worm-robot locomotion in a flexible environment: Theory and experiments. *IEEE Trans. Biomed. Eng.* **2012**, *59*, 1057–1067. [CrossRef]
32. Wang, X.; Meng, M.Q.H. An experimental study of resistant properties of the small intestine for an active capsule endoscope. *Proc. Inst. Mech. Eng.* **2010**, *224*, 107–118. [CrossRef]